

# A Multi-Scale Approach to Describe Electrical Impulses Propagating along Actin Filaments in both Intracellular and In-vitro Conditions

Christian Hunley, Diego Uribe, and Marcelo Marucho<sup>1</sup>

*Department of Physics and Astronomy, The University of Texas at San Antonio, San Antonio, TX 78249-5003*

---

## Abstract

An accurate and efficient characterization of the polyelectrolyte properties for cytoskeleton filaments are key to the molecular understanding of electrical signal propagation, bundle and network formation, as well as other relevant physicochemical processes associated with biological functions in eukaryotic cells and their potential nanotechnological applications. In this article, we introduce an innovative multi-scale approach able to account for the atomistic details of a proteins molecular structure, its biological environment, and their impact on electrical impulses propagating along wild type Actin filaments. The approach provides a novel, simple, accurate, approximate analytic expression for the characterization of electrical impulses in the shape of soliton waveforms. It has been successfully used to determine the effects of electrolyte conditions and voltage stimulus on the electrical impulse shape, attenuation and kern propagation velocity in these systems. It has been shown that the formulation is capable of accounting for the details of electro-osmosis and convection, as well as the electrical double layer of G-actins including the electrical conductivity and capacitance. The approach predicts higher electrical conductivity, linear capacitance and nonlinear accumulation of charge in intracellular condicions. Our results also show a significant influence of the voltage input on the electrical impulse shape, attenuation and propagation velocity. The filament is able to sustain the soliton propagation at almost constant kern velocity in the in-vitro condition, but the soliton displays a remarkable deceleration in the intracellular condition. Additionally, the solitons are narrower and travel faster at higher voltage input. Whereas, the voltage input does not play an important role on the soliton kern velocity in the in-vitro condition. Overall, Our results predict the propagation of electrical signal impulses in the form of solitons for the range of voltage stimulus and electrolyte solutions typically present in intracellular and in-vitro conditions. This multi-scale theory may also be applicable to other highly charged rod-like polyelectrolytes with relevance in biomedicine and biophysics. It is also able to account for molecular structure conformation (mutation) and biological environment (protonations/deprotonations) changes often present in pathological conditions.

---

**Keywords:** Electrical signal propagation, Actin filaments, Theoretical developments, Electrochemistry, Polyelectrolytes

---

<sup>1</sup>Email:marcelo.marucho@utsa.edu

## 1. Introduction

Actin filaments (F-actin) are long charged rod-like cytoskeleton polymers, which carry out many important biological activities in eukaryotic cells.<sup>1,2</sup> These microfilaments have recently gained wide notoriety for their fascinating polyelectrolyte properties.<sup>3</sup> According to single filament experiments in solution,<sup>4,5</sup> F-actin have been shown to sustain ionic conductance and transmit electrical currents in the form of localized counterionic waves about the polymer's surface. The velocity of propagation along the surface of an actin microfilament is consistent with the velocity of propagation for neuronal impulses. Hence, in principle, concurrent propagation of both electrical signals along actin microfilaments, and electrochemical currents along the axonal membrane are highly possible. Another intriguing property of these proteins is their capacity for overcoming electrostatic interactions to form higher-order structures (bundles and networks) in the cytoplasm. For instance, cytoskeletal filaments are often directly connected with both ionotropic and metabotropic types of membrane embedded receptors, thereby linking synaptic inputs to intracellular functions.<sup>6</sup> Conducting microfilaments may also govern at least some aspects of overall ion channel behavior within microvilli.<sup>7,8</sup>

All of these observations provide strong evidence on the polyelectrolyte nature of F-actin, which provides unique, yet still poorly understood, conducting and bundling formation properties in a variety of neuron activities including intracellular information processing, regulating developmental plasticity, and mediating transport. Certainly, the molecular understanding of the polyelectrolyte properties of cytoskeleton filaments will not only open unexplored frontiers in biology and biomedicine, but it will also be crucial for the development of reliable, highly functioning small devices with biotechnological applications such as bionanosensors and computing bionanoprocessors.<sup>9-13</sup> Therefore, it is of crucial importance to determine the underlying biophysical principles and molecular mechanisms that support the ionic conductance and electrical impulse transmission in Actin filaments under a variety of biological environments.

The current understanding of these phenomena builds on a pioneers work, Fumio Oosawa suggested around 50 years ago that electric signals could be channeled through a medium along a microfilament due to the electrolyte solution forming an electron cloud along the filament length<sup>14</sup>. It was Manning who introduced condensation theory<sup>15</sup>, which provided the foundation for linear polymers to enable electrical currents in the form of ionic movements. As charged polyelectrolytes, cytoskeleton filaments may contain a proportion of their surrounding counterions in the form of a dense or "condensed" cloud about their surface, as long as, there is a sufficiently high linear charge density, a critical concentration of multivalent ions, and a small dielectric constant of the surrounding medium. These criteria are indeed met for actin filaments in neurons.<sup>14,16,17</sup> Further, molecular structure analysis indicates the distribution of counterion clouds is nonuniform along the filament's length. This is because F-actin originates from the linear polymerization of globular actin (G-actin) units. Each of these units have tight binding sites that mediate head-to-tail interactions to form a double-stranded helix. Therefore, resembling a solenoid with a fluctuating current flowing as a result of voltage differences generated by the ends of the filament. Additionally, with the filament core separated from the rest of the ions in the bulk solution by the counterion condensation cloud, this overcast of counterions may act as a dielectric medium between the filament and bulk layer. Hence, providing F-actin both resistive and capacitive behaviors that may be associated with a highly conductive medium. This conduction along microfilaments is characterized by the decomposition of an electrical input pulse

into discrete delayed charge portions. These patterns clearly indicate the existence of charge centers with corresponding counter ion clouds along the polymer axis. As a consequence, electrically forced ions entering one end of the biopolymer will result in ions exiting the other end (Fig. 1). Therefore, actin polymers may serve as "electrical nanobio-wires" whom can be modeled as nonlinear inhomogeneous transmission lines known to propagate nonlinear dispersive solitary waves.<sup>18</sup> These waves can take the form of localized electrical signal impulses.<sup>19-21</sup> However, this basic understanding on electrical impulses propagating along actin filaments does not account for all conductance properties of microfilament bundles.<sup>22</sup> More recent approaches, based on Gouy-Chapman electrical double layer type models and mean-field Poisson-Boltzmann theories, provide further insight into the ionic equilibrium distributions and electric potential properties near the polymer surface, which arise from the charged polyelectrolyte surface, continuum solvent dielectric medium, and mean electrostatic potential energy generated by mixed salts comprised of point-like ions<sup>23-27</sup>. These methods are shown to break down for cytoskeleton filaments under certain situations, because they entail several approximations in their treatment of the ions and solvent molecules. They don't account for water crowding, ion size asymmetry or electrostatic ion correlation effects, all of which are likely to play a fundamental role in providing a quantitative description of the polyelectrolyte nature of cytoskeleton filaments, and consequently, their conducting and electrical signal propagation properties<sup>28-31</sup>.

In this article, we introduce a novel multi-scale (atomic( $\text{\AA}$ )  $\rightarrow$  monomer( $nm$ )  $\rightarrow$  filament( $\mu m$ )) approach to describe nonlinear dispersive electrical impulses propagating along Actin filaments (see Fig. 1). In section II, an atomistic model for the F-actin<sup>32</sup> and its biological environment is used to determine the polyelectrolyte properties and molecular mechanisms governing G-actins in the polymerization state. This approach, along with a suitable modification of Nernst-Planck theory<sup>33</sup>, are used to calculate the monomeric radial and axial flow resistances. In addition, a more sophisticated approach based on a classical solvation density functional theory<sup>31,34-37</sup> is required to calculate the monomeric radial ionic capacitance. In section III we use this monomer characterization to capture the biophysics and biochemistry at larger (microfilament) scale distances. We utilize those parameters in a nonlinear inhomogeneous transmission line prototype model which accounts for the monomer-monomer interactions, and consequently, the electrical impulse propagation along the filament length. A novel approximate analytic solution is obtained for this model and utilized in section IV to characterize the electrical impulse peak, width, and velocity of propagation under several voltage stimulus and electrolyte conditions.

## 2. G-actin Characterization in the Polymerization State

### 2.1. Cylindrical Biomolecule Model for G-actins

The physicochemical properties of each monomer composing the actin filament are different from those as single globular actin proteins, because polymerization into filamentous form generates several conformational changes on each monomer. Therefore, we retrieve the information on the monomer molecular structure from one of the most recent 13 monomers, biologically assembled wild type F-actin filament models posted on the protein data bank: the Cong model<sup>32</sup> (see Fig.2a). It provides a detailed molecular characterization including the amino acids sequence and the number and type of residues exposed to the electrolyte. This uncharged molecular structure in pdb format is uploaded into pdb2pqr webserver<sup>38</sup> to assign atomic charges and sizes, add hydrogens, optimize the hydrogen bonding network, and renormalize atomic charges

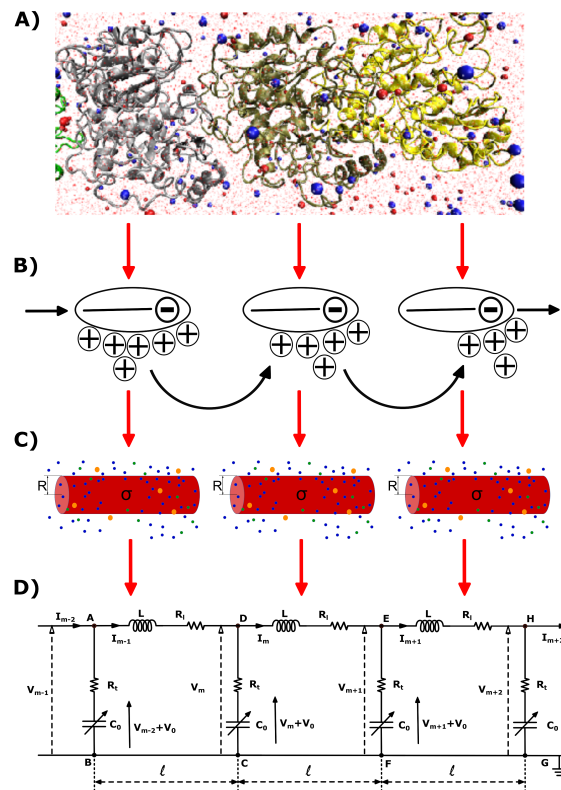


Figure 1: A) Molecular Structure Model. B) Ion Condensation Theory. C) Cylindrical Biomolecule Model D) Dispersive Transmission Line Model

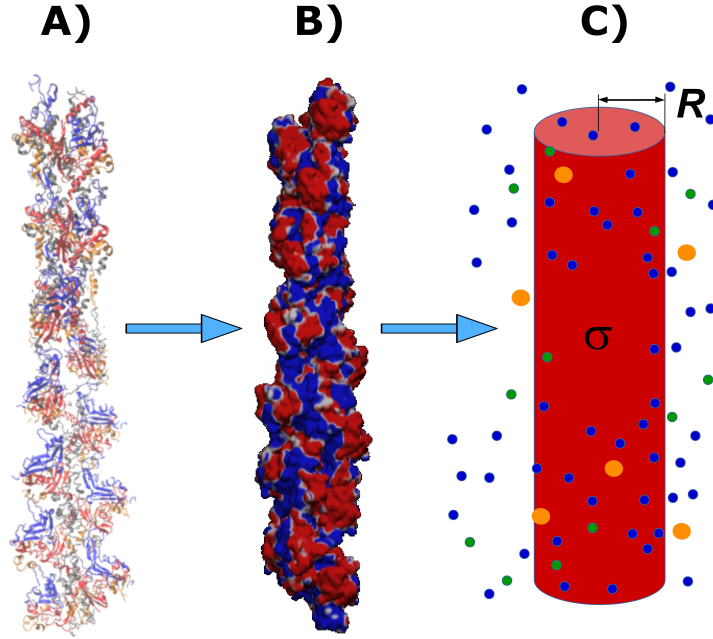


Figure 2: A) Cong Model B) Filament Volume C) Cylindrical Characterization

of the residues exposed to the surface due to pH effects (protonation/deprotonation process). The resulting charged molecular structure at  $pH = 7.2$  is used to extract information on the effective filament  $L = Z_{max} - Z_{min} = 422.20\text{\AA}$  and monomer length  $\ell = L/13 = 5.4nm$ , as well as the total filament charge  $Q = \sum q_i = -154e$ , where  $e$  is the electronic charge (see Fig. 2b). The filament length and total charge are used to estimate the filament linear charge density  $\lambda = Q/L = -0.365\frac{e}{\text{\AA}}$ . The resulting structure is uploaded into “3v: voss volume voxelator” web-server<sup>39</sup> to estimate the total filament volume  $V_p = 753005\text{\AA}^3$ . From here the effective monomer radius  $R$  of the molecular structure model is calculated  $R = \sqrt{V_p/(2L)} = 23.83\text{\AA}$ . The linear charge density and radius are subsequently used to calculate the filament (= monomer) surface charge density  $\sigma = \lambda/(2\pi R) = -0.039027\frac{C}{m^2}$ . This effective radius  $R$ , length  $\ell$  and surface charge density  $\sigma$  are used in the next sections to determine the longitudinal and transversal ionic flow resistances, capacitance and self-inductance for each monomer along the filament length ((see Fig. 2c).

## 2.2. Electrical and Conductive Properties of G-actins in Solutions

In this approach, the electrical properties of a single G-actin are characterized by a capacitor, two resistances and a self-inductance component. The capacitor, whose capacitance changes with applied voltage, originates the non-linearity behavior of the electrical impulse. The structural periodicity in the arrangement of monomers generates the dispersion of the electrical impulse along the filament. Whereas, the losses in the transmission media is accounted for by a series and shunt resistors, which represent the finite conductivity of the conductors and the dielectric insulator between the conductors, respectively. Additionally, the inductive component to the electrical properties of the electrical impulse is due to F-actin’s double-stranded helical structure, which induces the ionic flow in a solenoidal manner around each monomers. A detailed

characterization of these properties is provided below.

### 2.2.1. Longitudinal and Transversal Ionic Flow Resistances

We use transport and Ohm's laws as well as Navier-Stokes and Poisson's theories to obtain simple and accurate, approximate analytic expressions for the radial (transversal) and axial (longitudinal) ionic flow resistances. To make calculations tractable, we assume azimuthal and axial symmetry on the electric potential generated by charged ions and monomer surface charge densities. We also assume that the radial electrolyte convection is neglectable.

In the longitudinal ionic flow resistance calculations, we also assume that an external perturbation voltage  $\Delta V$  is applied between the monomer ends, which are separated by a distance  $\ell$ . This voltage drop generates a uniform axial electric field along the monomer with magnitude  $E_z = \frac{|\Delta V|}{\ell}$ , and consequently, an electro-osmotic (migration) force on the ions in the electrolyte. Another longitudinal driving force considered in this approach is the natural convection arising from the movement of the fluid characterized by the axial velocity profile  $v_z(r)$ . As a result, the transport law provides the following equation for the axial electric surface current density<sup>23</sup>

$$i_z(r) = k(r)E_z + v_z(r)\rho_e(r) \quad r \geq r_\xi > R \quad (1)$$

This expression depends on the electrolyte conductivity

$$k(r) = F^2 \sum_i z_i^2 u_i c_i(r) \quad (2)$$

and the total charge density distribution

$$\rho_e(r) = F \sum_i z_i c_i(r) \quad (3)$$

In previous expressions,  $r_\xi \simeq R$  is the slip velocity position,  $v_z(r_\xi) = 0$ ,  $F$  is Faraday's constant and the mobility, valence, and concentration of ion species  $i$  are represented by  $u_i$ ,  $z_i$ , and  $c_i(r)$ , respectively.

Moreover, we combine Poisson's and the Navier-Stokes' equations to obtain the following expression for the axial velocity profile

$$v_z(r) = \frac{\epsilon E_z}{\mu} [\phi(r) - \phi(r_\xi)] \quad r \geq r_\xi. \quad (4)$$

This expression indicates that under the action of a uniform axial electric field, the velocity profile of the fluid is proportional to the radial electric potential drop  $\phi(r) - \phi(r_\xi)$ . In the latter equation,  $\epsilon = 7.0832 \cdot 10^{-10} \frac{F}{m}$  and  $\mu = 0.00089 \frac{Kg}{m.s}$  represent the absolute bulk permittivity and viscosity parameters, respectively. On the other hand, the radial electric potential  $\phi(r)$  is generated by the total charge density distribution as dictated by the Poisson's equation

$$\rho_e(r) = -\frac{\epsilon}{r} \frac{\partial}{\partial r} \left( r \frac{\partial \phi(r)}{\partial r} \right) \quad (5)$$

To obtain an analytic solution for the electric potential we use a Boltzmann distribution and Debye-Hückel (linearized PB) approximation for the ion density distributions

$$c_i(r) = c_i^\infty \exp \left[ -\frac{z_i F \phi(r)}{RT} \right] \approx c_i^\infty \left( 1 - \frac{z_i F \phi(r)}{RT} \right), \quad \left| \frac{z_i F \phi(r)}{RT} \right| \ll 1 \quad (6)$$

where  $c_i^\infty$  is the bulk concentration of species  $i$  [ $\frac{\text{mol}}{\text{m}^3}$ ],  $R$  the gas constant, and  $T$  the electrolyte temperature. After substitution of eqn (6) into eqn (3), the use of the bulk electroneutrality condition ( $\sum_i z_i c_i^\infty = 0$ ), and the replacement of the resulting expression into eqn (5), we obtain

$$\phi(r) = \frac{\sigma \lambda K_0 \left( \frac{r}{\lambda} \right)}{\epsilon K_1 \left( \frac{r_\xi}{\lambda} \right)} \quad r > R \quad (7)$$

where  $K$  is the modified Bessel function of the second kind,  $\lambda$  represents the Debye length  $\lambda = (\epsilon RT / (F^2 \sum_i z_i^2 c_i^\infty))^{1/2}$ ,  $\sigma$  the monomer surface charge density,  $r$  is the radius predicted by the cylindrical model. Note that the Debye length in eqn (7) plays an important role providing an estimate on the width of the electrical double layer.

The approximate analytic solution obtained for the electric potential  $\phi(r)$  is subsequently replaced into eqn (6), (5), (4), and (2) to get an analytic solution for the surface current density. This solution is integrated over the Bjerrum length  $\ell_b = \frac{e^2}{4\pi\epsilon\epsilon_0 k_b T} = 6.738 \text{ \AA}$ , e.g. the length scale below which electrostatic correlations are important. In the latter expressions,  $\epsilon = 80$  is the relative bulk solvent dielectric constant;  $\epsilon_0 = 8.854 \cdot 10^{-12} [\frac{F}{m}]$  the vacuum permittivity;  $k_b = 1.381 \cdot 10^{-23} [\frac{J}{K}]$  the Boltzmann's constant, and  $T$  the temperature in Kelvin degree. The integration yields the following expression for the total longitudinal ionic current

$$\frac{I_l}{2\pi} = E_z \int_{r_\xi}^{\ell_b+r_\xi} r k(r) dr + \int_{r_\xi}^{\ell_b+r_\xi} r v(z) \rho_e(r) dr \quad (8)$$

After performing some algebra and integral calculations using mathematica11.1 software<sup>40</sup> expression 8 becomes

$$I_l = E_z \pi ((\ell_b + r_\xi)^2 - r_\xi^2) \{k^\infty + \Delta k_l\} = \frac{|\Delta V|}{\ell} \pi ((\ell_b + r_\xi)^2 - r_\xi^2) \{k^\infty + \Delta k_l\} \quad (9)$$

where  $k^\infty$  is the bulk electrolyte conductivity

$$k^\infty = F^2 \sum_i z_i^2 u_i c_i^\infty, \quad (10)$$

$\Delta k_l$  the corrections predicted by our approach

$$\Delta k_l = -\frac{2F^3 \sigma \lambda^2 r_\xi \sum_i z_i^3 u_i c_i^\infty}{\epsilon RT ((\ell_b + r_\xi)^2 - r_\xi^2)} \left( 1 - \frac{(\ell_b + r_\xi) K_1 \left( \frac{\ell_b + r_\xi}{\lambda} \right)}{r_\xi K_1 \left( \frac{r_\xi}{\lambda} \right)} \right) + \frac{r_\xi^2 \sigma^2}{\mu ((\ell_b + r_\xi)^2 - r_\xi^2)} G(\ell_b, r_\xi, \lambda) \quad (11)$$

and  $G$  is the following analytic function

$$G(\ell_b, r_\xi, \lambda) \left[ K_1 \left( \frac{r_\xi}{\lambda} \right) \right]^2 = \left\{ \left( K_0 \left( \frac{r_\xi}{\lambda} \right)^2 - K_1 \left( \frac{r_\xi}{\lambda} \right)^2 \right) + 2 \frac{\lambda}{r_\xi} K_0 \left( \frac{r_\xi}{\lambda} \right) K_1 \left( \frac{r_\xi}{\lambda} \right) \right. \\ \left. - \frac{(\ell_b + r_\xi)^2 \left( K_0 \left( \frac{(\ell_b + r_\xi)}{\lambda} \right)^2 - K_1 \left( \frac{(\ell_b + r_\xi)}{\lambda} \right)^2 \right) - 2 \frac{\lambda(\ell_b + r_\xi)}{r_\xi^2} K_0 \left( \frac{(\ell_b + r_\xi)}{\lambda} \right) K_1 \left( \frac{(\ell_b + r_\xi)}{\lambda} \right)}{r_\xi^2} \right\}.$$

Finally, the longitudinal ionic flow resistance  $R_l$  is calculated from ohm's law, which relates the axial voltage drop  $\Delta V$  and the total electric current  $I$  as  $R_l = |\Delta V/I|$ . As a result, we have

$$R_l = \frac{\ell}{\pi \left( (\ell_b + r_\xi)^2 - r_\xi^2 \right) |k^\infty + \Delta k_l|} = \frac{\ell}{S_l \varrho_l}, \quad (12)$$

where  $S_l = \pi \left( (\ell_b + r_\xi)^2 - r_\xi^2 \right)$  represents the effective cross section surface area facing perpendicular to the longitudinal ionic flow and  $\varrho_l = |k^\infty + \Delta k_l|$  is the effective axial ionic conductivity.

A similar approach is used for the transversal ionic flow resistance calculations. Here we assume that the electro-osmosis generated by the gradient of the radial electric potential is the only driving (migration) force dominating the radial surface current density

$$i_r(r) = -F \sum_i z_i \left( F z_i u_i c_i(r) \frac{\partial \phi(r)}{\partial r} \right) \quad (13)$$

Since this expression does not depend on the axial and azimuthal coordinates, the total radial current  $I_r$  passing from the inner to the outer layer is obtained by multiplying the radial surface current density by the lateral monomeric surface layer area at a section  $r$  in the solution, e.g.  $I_r = i_r(r) 2\pi \ell r$ .<sup>23</sup> Since  $I_r$  is a constant independent of position, this expression can be integrated across the electrical double layer to obtain

$$\int_{r_\xi}^{\ell_b + r_\xi} \frac{I_r}{2\pi \ell r} dr = \int_{r_\xi}^{\ell_b + r_\xi} i_r(r) dr = -k^\infty \int_{r_\xi}^{\ell_b + r_\xi} \frac{\partial \phi(r)}{\partial r} dr + \frac{F^3}{RT} \sum_i z_i^3 u_i c_i^\infty \int_{r_\xi}^{\ell_b + r_\xi} \phi(r) \frac{\partial \phi(r)}{\partial r} dr \quad (14)$$

Therefore,

$$\frac{I_r \ln \left( \frac{\ell_b + r_\xi}{r_\xi} \right)}{2\pi \ell} = -k^\infty [\phi(\ell_b + r_\xi) - \phi(r_\xi)] + \frac{F^3}{2RT} \sum_i z_i^3 u_i c_i^\infty [\phi^2(\ell_b + r_\xi) - \phi^2(r_\xi)]$$

After some algebra we obtain a linear dependence between the total radial current  $I_r$  and the electric potential drop across the electrical double layer  $\Delta \phi \equiv \phi(r_\xi) - \phi(\ell_b + r_\xi)$  following the Ohm-like law equation

$$\frac{I_r \ln \left( \frac{\ell_b + r_\xi}{r_\xi} \right)}{2\pi \ell \left[ k^\infty - \frac{F^3}{2RT} \sum_i z_i^3 u_i c_i^\infty [\phi(\ell_b + r_\xi) + \phi(r_\xi)] \right]} \equiv I_r R_t = \Delta \phi$$



where the radial ionic flow resistance is given by

$$R_t = \frac{\ln\left(\frac{\ell_b + r_\xi}{r_\xi}\right)}{2\pi\ell\left|k^\infty - \frac{F^3}{2RT}\sum_i z_i^3 u_i c_i^\infty [\phi(\ell_b + r_\xi) + \phi(r_\xi)]\right|} = \frac{\ell_b}{2\pi\ell r_\xi |k^\infty + \Delta k_t|} = \frac{\ell_b}{S_t \varrho_t}, \quad (15)$$

In the later expression  $S_t = 2\pi\ell r_\xi$  represents the effective lateral surface area facing perpendicular to the radial ionic flow,  $\varrho_t = |k^\infty + \Delta k_t|$  is the effective radial ionic conductivity, and  $\Delta k_t$  the corrections to the bulk electrolyte conductivity

$$\Delta k_t = k^\infty \left\{ \frac{\ell_b}{r_\xi \ln\left(\frac{\ell_b + r_\xi}{r_\xi}\right)} - 1 \right\} - \frac{\ell_b \sigma \lambda F^3 \sum_i z_i^3 u_i c_i^\infty}{2r_\xi RT \epsilon K_1 \left(\frac{r_\xi}{\lambda}\right) \ln\left(\frac{\ell_b + r_\xi}{r_\xi}\right)} \left[ K_0\left(\frac{(\ell_b + r_\xi)}{\lambda}\right) + K_0\left(\frac{r_\xi}{\lambda}\right) \right] \quad (16)$$

We note that our results recover more oversimplified approximations for cytoskeleton filaments when these contributions are neglected,<sup>24,25</sup> namely

$$R_l \simeq R_l^o = \frac{\ell}{2\pi\ell_b r_\xi k^\infty}, \quad R_t \simeq R_t^o = \frac{\ell_b}{2\pi\ell r_\xi k^\infty}, \quad \ell_b \ll r_\xi, \quad \sigma = 0, \quad c_i^\infty \ll 1.$$

Additionally, under the conditions considered in this article,  $\ell_b \lesssim \lambda$ , which is needed to justify a mean-field theory for the diffuse part of the electrical double layer.

### 2.2.2. Ionic Capacitance

The Poisson-Boltzmann theory used in the previous calculations is certainly inaccurate to describe the differential capacitance of electric double layers in ionic liquids and its correlation with the monomer surface charge density and electric potential.<sup>28,29</sup> In the present article, we use a more sophisticated approach based on a classical solvation density functional theory (CSDFT).<sup>34</sup> The polyelectrolyte properties of the biomolecule are characterized by the effective molecular radius  $R$  and uniform bare surface charge density  $\sigma$  predicted by the Cong molecular structure model, whereas the biological environment is represented by an electrolyte (either alkaline, acid or neutral) solution comprised of ionic species (characterized by crystal radius,<sup>41</sup> charge and bulk concentration), explicit water molecules (characterized by neutral ions at experimental size (2.75Å) and bulk concentration (55.56M)) (Fig. 2). The approach was successfully tested on segments of B-DNAs and its application is extended here to describe the polyelectrolyte properties of a segment of F-actin (e.g., a monomer)..

To calculate the capacitance of the cylindrical electrical double layer we consider a monomer perturbed by changing the pH level (alkaline, acid and neutral levels) in the solution. These pH changes generate perturbations on the surface charge density  $\sigma$ , which are predicted by the Cong molecular structure model and titration calculations as explained previously. For each surface charge density value we use CSDFT to predict the induced changes on the corresponding surface electrical potential  $\psi_o$ . These two sets of parameter values can be correlated using a cubic fitting polynomial curve. These curves are used to calculate the slope analytically to obtain the following expression for the differential capacitance  $C_d$

$$C_d = \frac{d\sigma}{d\psi_o} = \widehat{C}_o \left( 1 - 2\widehat{b}\psi_o + 3\widehat{c}\psi_o^2 + \mathcal{O}(\psi_o^3) \right) \quad (17)$$

Integration of this expression with respect to the electric potential along the voltage drop  $V$  across the electrical double layer leads to the following expression for the total charge accumulated in the capacitor<sup>42</sup>

$$Q = 2\pi r_\xi \ell \hat{C}_o (V - \hat{b}V^2) = C_o (V - bV^2) = VC_o(1 - bV) = VC(V) \quad (18)$$

where  $C_o$  represents the linear capacitance of the capacitor and  $b$  the theory's parameter characterizing its nonlinear behavior. Specific values for these parameters in intracellular and in-vitro conditions are provided below.

### 2.2.3. Self-Inductance

In reference (24) Faraday's law is used to estimate the self-inductance  $L$  for G-actins which is found to be of the order of pico-Henry

$$L = \frac{\Gamma N^2 \pi (r_\xi + \lambda)^2}{\ell} \simeq 1.2 \cdot 10^{-17} F \quad (19)$$

where  $\Gamma$  and  $N$  represent the magnetic permeability and the number of turns (e.g. how many ions could be lined up along the length of a monomer), respectively. Here  $N \simeq d/\ell$ , where  $d$  is the average ion size.

According to this result, the contribution to the electrical signal propagation for F-actins is expected to be neglectable, however it may play an important role in other highly charged filaments. Therefore, in the present work we include this rough estimate of self-inductance in the approach.

## 3. Lossy, Nonlinear, Dispersive Transmission Line Model for Microfilaments

Loan counterions surrounding microfilaments may be transferred from one charge center (e.g. monomer) to the next, giving rise to locally restricted excess of partial charges representing the propagation of electrical impulses along the conducting pathway.<sup>8</sup> This kind of charge transfer mechanism between monomers is well known to generate flow of weakly bound electrons in conducting polymer systems where the electrical current and propagation velocity are different in nature. These transmission line models have been successfully demonstrated to characterize electron currents along conducting polymers, and are often utilized to describe ionic conductance and electrical impulse propagation along cytoskeleton filaments.<sup>18,26,43</sup> Here we use the sequential arrangement of elementary electric units introduced in references.<sup>24</sup> In this case, each unit represents a single G-actin characterized by the capacitor, resistances and self-inductance described in the previous section.

Application of Kirchoff's laws on the discrete transmission line model constructed by  $N$  elementary cells (monomers) provides a differential equation for describing the electric potential and ionic current across cell units. The current conservation law at the node A between the cells " $m - 1$ " and " $m$ ", provide the following equation (see Fig. 3)

$$I_{m-1} - I_m = \frac{\partial Q_m}{\partial t} \quad (20)$$

where  $\partial Q_m/\partial t$  represents the current across the capacitor in the cell " $m$ ". By replacing eqn (18) into eqn (20) we have

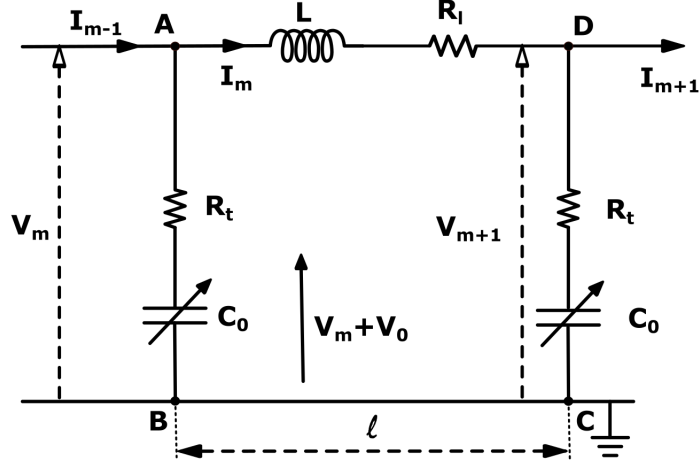


Figure 3: Effective circuit diagram for the  $m^{\text{th}}$  monomer

$$I_{m-1} - I_m = C_o \left( \frac{\partial V_m}{\partial t} - 2bV_m \frac{\partial V_m}{\partial t} \right) \quad (21)$$

On the other hand, Kirchoff's voltage law along the circuit ABCD generates the following expression (see Fig. 3)

$$v_m - v_{m+1} = L \frac{\partial I_m}{\partial t} + I_m R_l \quad (22)$$

where  $v_m$  is given by

$$v_m = R_t (I_{m-1} - I_m) + V_o + V_m \quad (23)$$

and  $V_o$  represents a constant DC bias electric potential. Further substitution of eqn (23) into eqn (22) yields

$$L \frac{\partial I_m}{\partial t} + I_m R_l = R_t (I_{m-1} - 2I_m + I_{m+1}) + (V_m - V_{m+1}) \quad (24)$$

The later equation can be written in terms of the characteristic impedance of the electrical circuit unit  $Z$  and the new function  $U_m(t)$ , where as usual:<sup>26</sup>  $Z^{-1/2}U_m = I_m$  and  $Z^{1/2}U_m = V_m$ . In this article, the characteristic impedance is estimated as follows

$$Z \simeq \sqrt{R_{equiv}^2 + X_{equiv}^2} \quad (25)$$

where  $R_{equiv} = R_l + R_t$ ,  $X_{equiv} = \frac{T_o^{G-actin}}{2\pi C_o}$ , and  $T_o^{G-actin}$  is a parameter characterizing the electrical circuit unit time scale.

These expressions, when replaced into eqn (21) and (24), lead to the following coupled equations

$$U_{m-1} - U_m = C_o Z \left( \frac{\partial U_m}{\partial t} - 2bZ^{1/2}U_m \frac{\partial U_m}{\partial t} \right) \quad (26)$$

$$U_m - U_{m+1} = Z^{-1} \left[ L \frac{\partial U_m}{\partial t} + U_m R_l - R_t (U_{m+1} - 2U_m + U_{m-1}) \right] \quad (27)$$

Since F-actins are a filamentous form of its subunits g-actin, we have that the individual monomer length  $l$  is much smaller than the filament length  $(N - 1)l$ . As a result, we can approximate eqn (26) and (27) as the voltage  $V_m$  and current  $I_m$  travel down the actin filament by moving from one adjacent circuit modeled monomer to the next. Using the continuum approximation  $U_m(t) \simeq U(x, t)$  with a Taylor series in terms of the parameter  $\ell$  we obtain the following expansion for  $U_{m\pm 1}(t)$

$$U_{m\pm 1} = U(x \pm \ell, t) \simeq U \pm \ell \frac{\partial U}{\partial x} + \frac{\ell^2}{2} \frac{\partial^2 U}{\partial x^2} \pm \frac{\ell^3}{3!} \frac{\partial^3 U}{\partial x^3} \quad (28)$$

Consequently,

$$U_{m+1} - 2U_m + U_{m-1} = \ell^2 \frac{\partial^2 U}{\partial x^2} \quad (29)$$

$$U_{m-1} - U_{m+1} = -2\ell \frac{\partial U}{\partial x} - \frac{\ell^3}{3} \frac{\partial^3 U}{\partial x^3} \quad (30)$$

By summing eqn (26), (27), and using eqn (29) and (30) we have

$$Z^{-1} \left[ L \frac{\partial U}{\partial t} + U R_l - R_t \left( \ell^2 \frac{\partial^2 U}{\partial x^2} \right) \right] + C_0 \left( Z \frac{\partial U}{\partial t} - 2bZ^{3/2} U \frac{\partial U}{\partial t} \right) = -2\ell \frac{\partial U}{\partial x} - \frac{\ell^3}{3} \frac{\partial^3 U}{\partial x^3} \quad (31)$$

The later equation can be conveniently rewritten as follows

$$\left[ \frac{L}{Z} + C_0 Z \right] \frac{\partial U}{\partial t} + \frac{R_l}{Z} U - \frac{R_t \ell^2}{Z} \frac{\partial^2 U}{\partial x^2} - 2bZ^{3/2} C_0 U \frac{\partial U}{\partial t} + 2\ell \frac{\partial U}{\partial x} + \frac{\ell^3}{3} \frac{\partial^3 U}{\partial x^3} = 0 \quad (32)$$

The master equation (32) can be solved for  $U(x, t) = U(x(\xi, \tau), t(\tau)) = U(\xi, \tau)$  in terms of dimensionless variables

$$\xi = \frac{x}{\beta} - \frac{t}{\alpha}, \quad \tau = \frac{t}{24\alpha}, \quad \text{where} \quad \alpha = \frac{L}{Z} + C_0 Z > 0, \quad \text{and} \quad \beta = 2\ell, \quad (33)$$

After some manipulations and using the following relationships  $\frac{\partial}{\partial t} = \frac{1}{\alpha} \left( \frac{\partial}{\partial \tau} - \frac{\partial}{\partial \xi} \right)$ ,  $\frac{\partial}{\partial x} = \frac{1}{\beta} \frac{\partial}{\partial \xi}$ ,  $\frac{\partial^2}{\partial x^2} = \frac{1}{\beta^2} \frac{\partial^2}{\partial \xi^2}$  and  $\frac{\partial^3}{\partial x^3} = \frac{1}{\beta^3} \frac{\partial^3}{\partial \xi^3}$ , we have

$$\frac{\gamma \partial U}{24 \partial \tau} + \frac{\gamma R_l}{Z} U - \frac{\gamma R_t}{4Z} \left( \frac{\partial^2 U}{\partial \xi^2} \right) + 6U \left( \frac{\partial U}{\partial \xi} - \frac{\partial U}{\partial \tau} \right) + \frac{\gamma}{24} \frac{\partial^3 U}{\partial \xi^3} = 0 \quad (34)$$

where  $\gamma = \frac{3\alpha}{bZ^{3/2}C_0}$ . Since we look for slow changes on the time evolution in the electrical impulse solution of eqn (34),  $\frac{1}{24} \frac{\partial U}{\partial \tau} \ll \frac{\partial U}{\partial \xi}$ , the time rate in the electrical impulse is considered to be much slower than on the traveling variable. As a result, an analytic solution of eqn (34) can be obtained by performing the change,  $U = -\frac{\gamma}{24}W$  and defining new parameters  $\mu_2 = \frac{6R_t}{Z}$ ,  $\mu_3 = \frac{24R_l}{Z}$ . Accordingly, eqn (34) becomes the well-known perturbed Korteweg-de Vries (pKdV) differential equation<sup>21,44</sup>

$$\frac{\partial W}{\partial \tau} - 6W \frac{\partial W}{\partial \xi} + \frac{\partial^3 W}{\partial \xi^3} = \mu_2 \frac{\partial^2 W}{\partial \xi^2} - \mu_3 W \equiv P(W) \quad (35)$$

The left and right sides in the later equation represent the regular KdV equation<sup>45</sup> and the corresponding perturbation, respectively. The first term to the left resembles the time dependent term in Fick's diffusion law, whereas the second and third terms represent the non-linearity and dispersive contributions arising from the condensed ion cloud in the electrical double layer and the diffusive spreading of ions along the microfilament, respectively. On the other hand, the first and second terms to the right represent the dissipation and damping perturbations, respectively.

Equation (35) appears in a variety of systems<sup>46</sup> describing the propagation of electrical solitons in a nonlinear dispersive transmission line in the form of localized voltage waves. An initial pulse  $W(\xi, 0)$  in the transmission line may decay into a sequence of solitons and a tail. In this work, we will consider single soliton solutions only. In doing so, we assume that the perturbation is so small that it has a negligible influence on the soliton formation. Therefore, the perturbation will manifest itself by affecting the soliton only after an extended amount of time from its origination. Thus, the mutual interaction between solitons becomes unimportant when the soliton movement is of the order of its length. In what follows we consider this problem in the first approximation. In this case, the solution of equation (35) for non-dissipative systems ( $R_l = R_t = 0$ ) represents a non perturbed pulse soliton of the regular KdV equation<sup>(47)</sup>

$$W_{np}(\xi, \tau) = -2\Omega_0^2 \text{sech}^2 [\Omega_0 (\xi - 4\Omega_0^2 \tau)] \quad (36)$$

with dimensionless constant voltage amplitude  $2\Omega_0^2$  and propagation velocity  $4\Omega_0^2$ . Solitary-wave solutions that propagate without changing form may also be expected due to a balance between non-linearity and dispersion (e.g.  $|P(W)| \simeq 0$ ), hence requiring that the effect of the perturbing terms on the shape of the soliton cancel each other out.<sup>48</sup> Otherwise, when  $\mu_2$  and/or  $\mu_3$  are not zero, equation (36) is no longer the solution of the perturbed KdV equation.<sup>45,47,49,50</sup>

In this analysis, we look for an analytic solution of eqn (36) in the framework of the perturbation theory on the basis of the adiabatic approximation.<sup>47</sup> In that case, the solution is a soliton pulse  $W(\xi, \tau)$  in the form :

$$W(\xi, \tau) = -2 [\Omega(\tau)]^2 \text{sech}^2 [\Omega(\tau) (\xi - \eta(\tau))] \quad (37)$$

where  $\Omega(\tau)$  and  $\eta(\tau)$  satisfy the following equations

$$\frac{d\Omega}{d\tau} = -\frac{1}{4\Omega} \int_{-\infty}^{\infty} P(W) \text{sech}^2 z dz, \quad (38)$$

$$\frac{d\eta}{d\tau} = 4\Omega^2 - \frac{1}{4\Omega^3} \int_{-\infty}^{\infty} P(W) \left[ z + \frac{1}{2} \sinh(2z) \right] \operatorname{sech}^2 z dz, \quad (39)$$

$z = \Omega(\tau) (\xi - \eta(\tau))$  and  $P(W)$  is the perturbation term defined in eqn (35). The calculation of the integrals appearing in eqn (38) and (39) provide the following analytic solutions

$$\begin{aligned} \Omega(\tau) &= \Omega_0 \sqrt{\frac{\exp(-\frac{4\tau\mu_3}{3})}{1 + \frac{4\mu_2\Omega_0^2}{5\mu_3} (1 - \exp(-\frac{4\tau\mu_3}{3}))}} \equiv \Omega_0 M_1(\tau) \\ &\simeq \Omega_0 \left( 1 - \frac{2}{15} (4\mu_2\Omega_0^2 + 5\mu_3) \tau + \mathcal{O}\left(\left(\frac{4\tau\mu_3}{3}\right)^2\right) \right) \end{aligned} \quad (40)$$

$$\begin{aligned} \eta(\tau) &= -\frac{5}{4\mu_2} [4\mu_3\tau + 3 \log [5\mu_3]] \\ -\frac{5}{4\mu_2} \left[ -3 \log \left[ -4\Omega_0^2\mu_2 + \exp\left(\frac{4\tau\mu_3}{3}\right) (4\Omega_0^2\mu_2 + 5\mu_3) \right] \right] &\equiv 4\Omega_0^2\tau M_2(\tau) \\ &\simeq 4\Omega_0^2\tau \left( 1 - \frac{2}{15} (4\mu_2\Omega_0^2 + 5\mu_3) \tau + \mathcal{O}\left(\left(\frac{4\tau\mu_3}{3}\right)^2\right) \right) \end{aligned} \quad (41)$$

The validation of these expressions is discussed in Appendix A, where we provide a comparison between the exact numerical and our the approximate analytic solution.

Note that  $V = -\frac{\gamma\sqrt{Z}}{24}W$ , therefore the unperturbed dimensionless amplitude  $\Omega_0^2$  is linearly proportional to the external voltage input  $V_{inp}$

$$\Omega_0^2 = 24V_{inp}/(Z^{1/2} |\gamma|) \quad (42)$$

It is worth mentioning that eqn (40), (41) and (45) describe the evolution of one soliton in the presence of a perturbation characterized by the amplitudes  $M_1(\tau)$  and  $M_2(\tau)$  which are expected to yield a slow change on the soliton parameters.<sup>47</sup> Therefore, the expansions appearing in eqn (40) and (41) provide a good estimation of the characteristic soliton travel time (in seconds)  $T_0^{soliton} = \frac{360\alpha}{2(4\mu_2\Omega_0^2 + 5\mu_3)}$ . This time should be, in principle, larger than the characteristic

ion flow time, such that  $T_0^{soliton} \gtrsim T_0^{G-actin} = 2\pi C_o \sqrt{Z^2 - (R_l + R_t)^2}$ . Additionally, for the electrolyte conditions and models considered in the present article, we have  $\Omega_0^2 \lesssim 1$ ,  $L/Z \ll 1$  and  $R_t/R_l \ll 1$  which yield the following approximate implicit equation for the impedance

$$\frac{360\alpha}{2(4\mu_2\Omega_0^2 + 5\mu_3)} \simeq \left( \frac{3ZC_o}{16} \frac{Z}{R_l} \right) \gtrsim 2\pi C_o \sqrt{Z^2 - (R_l + R_t)^2} \simeq 2\pi C_o \sqrt{Z^2 - R_l^2}$$

with solution  $Z \gtrsim 25.1128R_l$  and  $T_0^{soliton} \gtrsim 50.1858\pi C_o R_l$ .

Another important soliton characterization is given by the expression for the kern velocity of the electrical impulse along the filament  $v(t)$  (in units of  $m/s$ ). By rewriting the argument of solution (37) in terms of the original variables we have

$$\Omega(\tau) (\xi - \eta(\tau)) = \frac{\Omega(\tau)}{\beta} \left( x - \left[ \frac{t}{\alpha} \beta + \beta \eta(\tau) \right] \right). \quad (43)$$

which provides the following expressions for the time dependent wave number  $k(t) = \frac{\Omega(t/(24\alpha))}{\beta}$  and kern propagation velocity

$$v(t) = \left( \frac{\beta}{\alpha} + \beta \frac{d\eta(\tau)}{dt} \right) = \frac{\beta}{\alpha} \left( 1 + \frac{1}{24} \frac{d\eta(\tau)}{d\tau} \Big|_{\tau=t/(24\alpha)} \right) \quad (44)$$

where

$$\frac{d\eta}{d\tau} = 4\Omega_0^2 \frac{\exp\left(-\frac{4\tau\mu_3}{3}\right)}{1 + \frac{4\mu_2\Omega_0^2}{5\mu_3} \left(1 - \exp\left(-\frac{4\tau\mu_3}{3}\right)\right)} \quad (45)$$

Based on these results, the time average kern velocity of the soliton in a time interval  $[0, t_{max}]$  can be calculated as usual

$$v_{av} = \langle v(t) \rangle = \frac{1}{t_{max}} \int_0^{t_{max}} v(t) dt \quad (46)$$

Here  $t_{max}$  represents the vanishing time, which in this work is considered as the time taken by the initial soliton amplitude to be attenuated 99%, namely  $[\Omega\left(\frac{t_{max}}{24\alpha}\right)/\Omega(0)]^2 = 0.01$ .

## 4. Results and Discussion

In this section, we use expressions (12), (15), (17), (19), (37), (40) and (41) to investigate the impact of different electrolyte solutions and voltage stimulus on the physicochemical properties of G-actins and electrical signal propagation along F-actins. We investigate two electrolyte solutions, one representing an intracellular biological environment in physiological solution conditions (140mM  $K^+$ , 4mM  $Cl^-$ , 75mM  $HPO_4^{2-}$ , and 012mM  $Na^+$  at 310 K),<sup>51</sup> whereas the other represents in vitro conditions<sup>5</sup> (0.1M  $K^+$  and 0.1M  $Cl^-$  at 298 K). For the voltage stimulus, we consider both 0.05V and 0.15V peak voltage inputs in order to simulate the typical electric potential present in cells and single microfilament experiments.

### 4.1. Model's Parameters

Our calculations on the Debye length reveal the formation of a wider electrical double layer in the intracellular condition than in-vitro condition, namely

$$\lambda = \begin{array}{ll} 6.587\text{\AA} & \text{intracellular fluid} \\ 9.902\text{\AA} & \text{in vitro} \end{array}$$

The effective conductivity predicted by our approach relative to the conventional results reads

$$\frac{\rho_t}{k^\infty} = \begin{array}{ll} |3.0736 - 2.1750| / 3.0736 = 0.292 & \text{intracellular fluid} \\ |1.4988 + 0.1512| / 1.4988 = 1.101 & \text{in vitro} \end{array}$$

$$\frac{\rho_l}{k^\infty} = \begin{array}{ll} |3.0736 - 1.376| / 3.0736 = 0.552 & \text{intracellular fluid} \\ |1.4988 + 0.776| / 1.4988 = 1.518 & \text{in vitro} \end{array}$$

with corresponding resistances

$$R_t = \begin{array}{l} \frac{1}{0.292} R_t^o = 3.4240 R_t^o = 8.71 M\Omega \quad \text{intracellular fluid} \\ \frac{1}{1.101} R_t^o = 0.908 R_t^o = 4.74 M\Omega \quad \text{in vitro} \end{array}$$

$$R_l = \begin{array}{l} \frac{1}{0.552} R_l^o = 1.8116 R_l^o = 261.35 M\Omega \quad \text{intracellular fluid} \\ \frac{1}{1.518} R_l^o = 0.6568 R_l^o = 195.00 M\Omega \quad \text{in vitro} \end{array}$$

and impedances

$$Z = \begin{array}{l} 6.55409 \cdot 10^9 \Omega \quad \text{intracellular fluid} \\ 4.89680 \cdot 10^9 \Omega \quad \text{in vitro} \end{array} ,$$

The results predicted on ion conductivity indicate an increase (decrease) of the resistances in typical in-vitro (intracellular) environments compared to the corresponding bulk values. These corrections, given by expressions (11), display a balance (competition) between migration and convection forces, which depend in a nontrivial fashion, on the electrical double layer thickness, the Debye length, the electrochemistry (particles electrophoresis mobility, valence, bulk density and size, solvent viscosity and dielectric permittivity), as well as the monomer surface chemistry (surface charge density and size).

Another neoteric result of this work is the prediction of the nonlinear charge accumulation due to the linear monomeric capacitance behavior, namely  $C(V) = C_o(1 - bV)$ . To obtain the numerical values of the parameters  $C_o$  and  $b$ , we correlate the set of surface charge densities values  $\sigma$  predicted by the Cong model with the set of surface electrical potentials values  $\psi_o$  predicted by CSDFT. We use the Fit function provided by mathematica software<sup>40</sup> to generate a cubic fitting polynomial between these two parameters as shown in Fig. 4. These curves, when used to calculate the slope analytically, generate the following value for  $C_o$  and  $b$

$$C_o = \begin{array}{l} 1.069 \cdot 10^{-16} F \quad \text{intracellular fluid} \\ 6.739 \cdot 10^{-17} F \quad \text{in vitro} \end{array}$$

$$b = \begin{array}{l} -9.446 V^{-1} \quad \text{intracellular fluid} \\ 0.4735 V^{-1} \quad \text{in vitro} \end{array}$$

The results on the capacitor show a remarkable increase in the linear capacitance in the intracellular condition, which has a high impact on the monomer's ability to accumulate electric energy in the capacitor. Additionally, the parameter  $b$  is negative for the intracellular condition, whereas it is positive for the in-vitro condition. Accordingly, the nonlinearity of the charge accumulated in the capacitor mimics the behavior of a nMOS varactor in accumulation mode and a diode<sup>52</sup> in our electric circuit unit model for the intracellular and in-vitro conditions, respectively. We note that the sign of the parameter  $b$  also affects the polarization of the transmission line voltage (soliton)  $V = -\frac{\gamma\sqrt{Z}}{24}W$ . Certainly, the following calculations

$$\gamma\sqrt{Z} = \frac{3\alpha}{bZ^{3/2}C_0} = \frac{3\left(\frac{L}{Z} + C_0Z\right)Z^{1/2}}{bZ^{3/2}C_0} \simeq \frac{3}{b} = \begin{array}{l} -0.3175V \quad \text{intracellular fluid} \\ 6.3356V \quad \text{in vitro} \end{array} \rightarrow V \simeq -\frac{1}{8b}W \quad (47)$$

predict that the electrical impulse will propagate upright and down for in-vitro and intracellular conditions, respectively. Another key role of this parameter arises from eqn (42) and (47) which



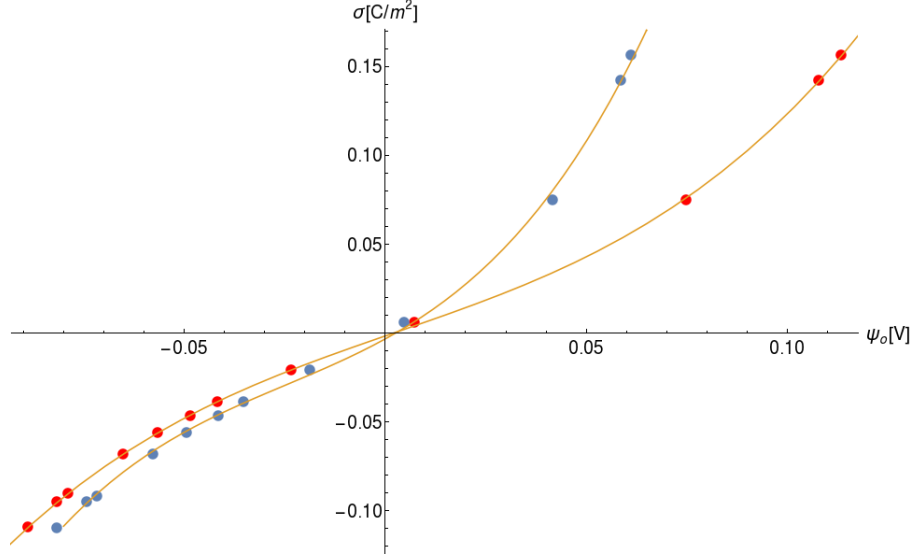


Figure 4: Monomer surface charge density as a function of the surface electric potential. Blue and red circles represent the data for intracellular and in-vitro conditions, respectively.

predict a linear dependence on the unperturbed soliton amplitude. Indeed, the substitution of these values for  $b$  into eqn (42) yields  $\Omega_0 = 1.3745$  and  $\Omega_0 = 2.3810$  (intracellular condition) and  $\Omega_0 = 0.30772$  and  $\Omega_0 = 0.5322$  (in-vitro condition), for  $0.05V$  and  $0.15V$  voltage inputs, respectively.

#### 4.2. Electrical Signal Propagation

We use expressions 37, 40 and 41 along with the numerical values for the parameters obtained previously to characterize the kern propagation velocity, shape and attenuation of the electrical impulse along an actin filament under a variety of conditions.

In Fig. 5, we illustrate the propagation of normalized electrical signals for  $0.15V$  voltage peak input for both intracellular and in-vitro conditions. Our results show similar soliton range of the order of a micron in both conditions. On the other hand, the soliton vanishing time is around 2 times longer in the intracellular condition. As a result, the biological environment has a high impact on the average kern propagation velocity and attenuation.

In Fig. 6, we compare several equitemporal snapshots of the soliton profile along F-actin for both electrolyte conditions and voltage peak inputs. In both biological conditions, the electrical impulse shape is wider for lower voltage inputs. Although, when comparing to each other, the shape of the soliton is narrower for the intracellular condition than for the in-vitro condition. The shift between consecutive blue and orange peak positions shown in Fig. 6a) indicates that solitons at higher voltage input travel faster in the intracellular condition. On the other hand, Fig. 6b) implies the voltage input does not play an important role on the soliton kern velocity for in-vitro condition. This is in agreement with the results displayed in Fig. 7 for the soliton kern velocity. Clearly, the filament is able to sustain the soliton propagation at almost constant kern velocity in the in-vitro condition (see Fig. 7b), namely  $v(0) \simeq v_{av} = 0.0328m/s$  and  $v(0) \simeq v_{av} = 0.0331m/s$  for  $0.05V$  and  $0.15V$  voltage inputs, respectively. Nevertheless, a different scenario is manifested in Fig. 7a) where the initial kern propagation velocity for the intracellular condition is

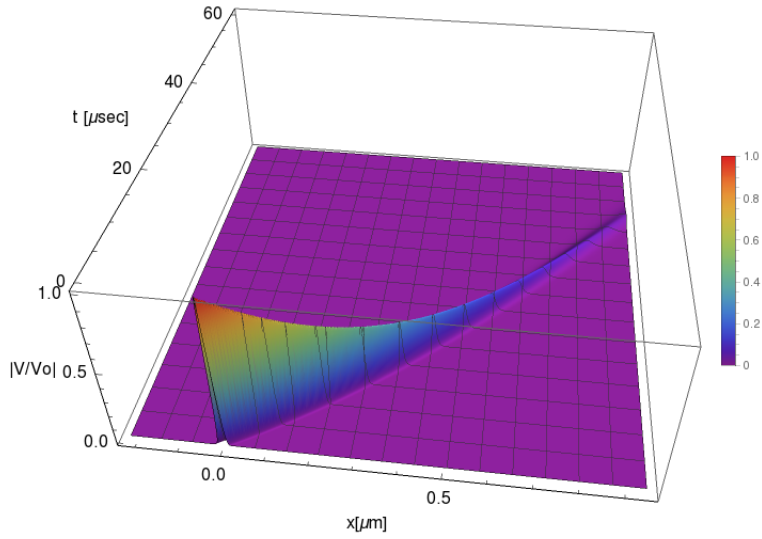
around  $v(0) = 0.03m/s$  and  $v(0) = 0.02m/s$  for  $0.05V$  and  $0.15V$  peak voltage inputs, respectively. The corresponding time averaged kern velocity is much lower, namely  $v_{av} = 0.01639m/s$  and  $v_{av} = 0.011853m/s$ . This indicates a remarkable soliton propagation deceleration caused by a larger linear capacitance and nonlinear parameter values, higher longitudinal ionic flow resistance, smaller electrical double layer thickness, and higher ion asymmetries (size, concentration, electrophoresis mobility, electrical valence, species number), among other factors. Additionally, our results demonstrate a higher voltage peak input that generates a higher time average kern propagation velocity. This can be understood from eqn (44) and (45), which predict an increasing propagation velocity of the electrical impulse with  $\Omega_0^2$ , and consequently, with the voltage input by expression (42). On the other hand, the time average velocity comparison between both electrolyte conditions reveal that solitons from the in-vitro condition travel, on average, faster than the intracellular condition, while the soliton peak attenuation is slower in the latter condition. This biological environment impact on electrical signal propagation is displayed in Fig. 8, which illustrates the soliton amplitude time evolution. It indicates similar vanishing time for both voltage peak inputs in each electrolyte condition. This is a consequence of the neglectable impact of the amplitude  $\Omega_0^2$  on the characteristic soliton travel time  $T_0^{soliton} = \frac{360\alpha}{2(4\mu_2\Omega_0^2+5\mu_3)} \simeq \frac{360\alpha}{10\mu_3}$ . Moreover, our results reveal a more pronounced, fast soliton attenuation decay rate at higher voltage input (blue lines in Fig. 8). This is caused by higher voltage inputs generating larger values for  $\Omega_0^2$ , and consequently, larger values for the denominator in eqn (40) for  $\Omega(t)$ .

Overall, our results predict that the propagation of electrical signal impulses in the form of solitons are possible for a range of electrolyte solution and voltage stimulus typically present in intracellular and in-vitro conditions. These predictions are in agreement with available experimental data on single Actin filaments.<sup>4,5</sup>

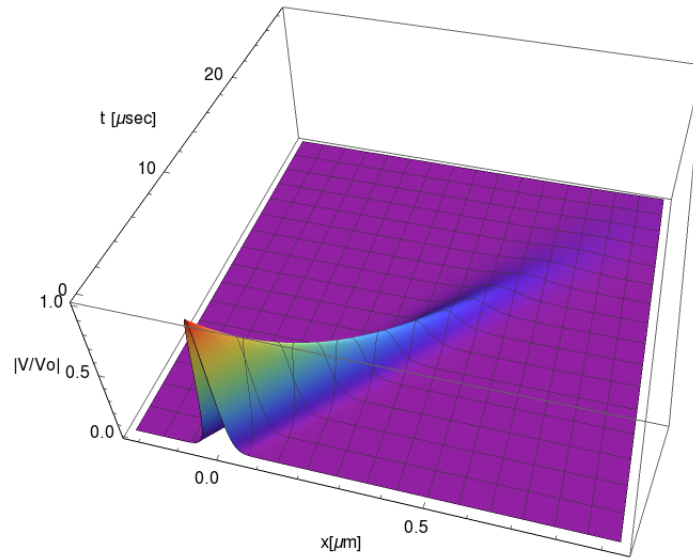
## 5. Conclusions

In this article, we introduced an innovative multi-scale approach which accounts for the atomistic details on the protein molecular structure and biological environment, as well as their impact on electrical impulses propagating in the form of micron solitons along wild type Actin filaments. The approach provides a novel, simple, accurate, approximate analytic expression for the characterization of solitons. It has been used to determine the effects of electrolyte conditions and voltage stimulus on the electrical impulse shape, attenuation and kern propagation velocity. The formulation has been shown to be capable of accounting for the details on the electrical double layer thickness and layering formation (ionic and water density distributions), the electrokinetics (particles electrophoresis mobility, valence and size, solvent viscosity and dielectric permittivity), and the monomer-electrolyte interface (surface charge density and size) on the ionic electrical conductivity and capacitance.

Our results reveal a high impact of the electrolyte condition on electrical conductivity and capacitance in G-actins. The approach predicts wider electrical double layer, higher electrical conductivity, linear capacitance and nonlinear accumulation of charge in intracellular conditions, which play an important role on the electrical signal propagation along the Actin filament. Additionally, the nonlinearity of the charge accumulated in the capacitor resembles the behavior of a varactor and a diode in our electric circuit unit model for the intracellular and in-vitro conditions, respectively. The approach also predicts different polarization of the transmission line

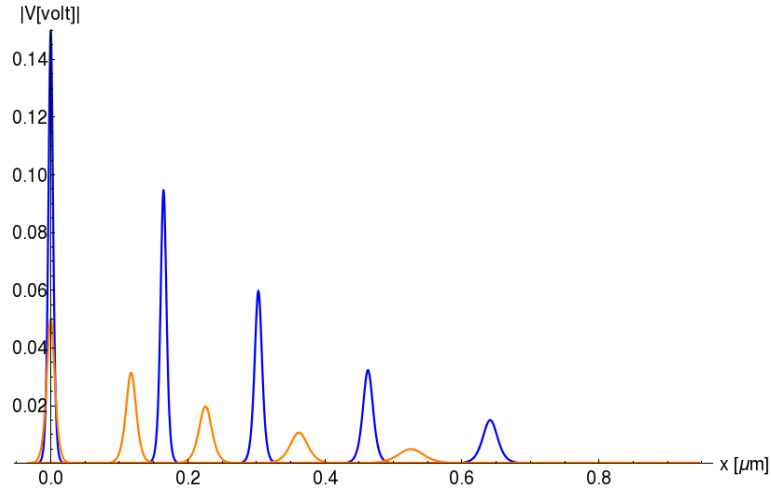


(a) Soliton traveling along F-actin in intracellular conditions

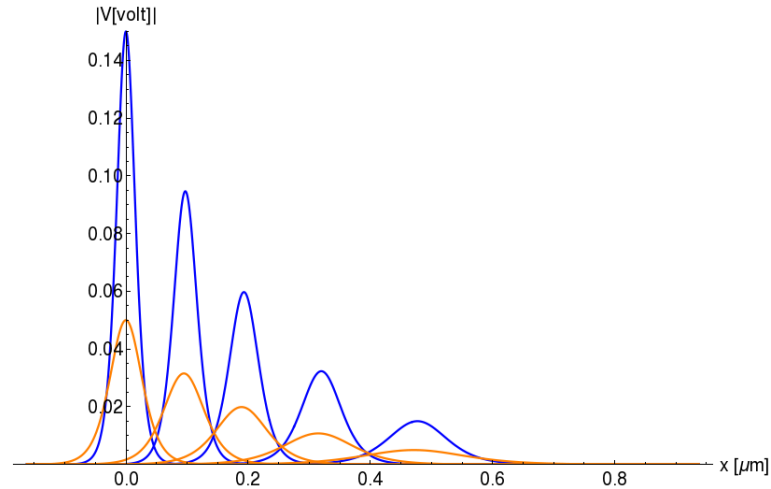


(b) Soliton traveling along F-actin in in-vitro conditions

Figure 5: Normalized Soliton solution  $|V(x, t)/V_o| = \left| W\left(\frac{x}{\beta} - \frac{t}{\alpha}, \frac{t}{24\alpha}\right) / (2\Omega_o^2) \right|$  for  $0.15V$  input voltage peak.

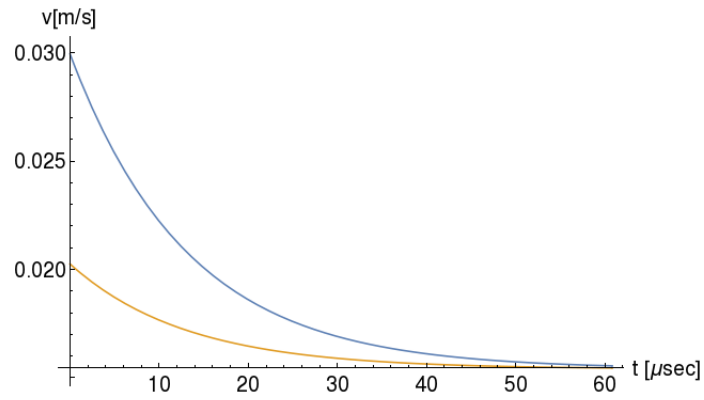


(a) Soliton profile along F-actin in intracellular conditions. The first, second, third, fourth and fiftieth peaks (same color) appearing from left to right correspond to the following snapshots  $t = 0\mu s$ ,  $t = 6\mu s$ ,  $t = 12\mu s$ ,  $t = 30\mu s$ , and  $t = 60\mu s$ , respectively.

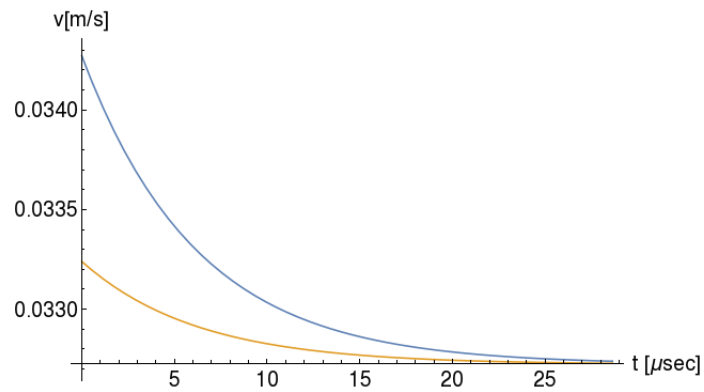


(b) Soliton profile along F-actin in in-vitro conditions. The first, second, third, fourth and fiftieth peaks (same color) appearing from left to right correspond to the following snapshots  $t = 0\mu s$ ,  $t = 2.8\mu s$ ,  $t = 5.7\mu s$ ,  $t = 14.3\mu s$ , and  $t = 28.6\mu s$ , respectively.

Figure 6: Snapshots of the Normalized soliton solution  $\left| \frac{V(x,t)}{V_o} \right| = \left| \frac{W\left(\frac{x}{\beta} - \frac{t}{\alpha}, \frac{t}{24\alpha}\right)}{2\Omega_o^2} \right|$ . Orange and blue colors represent the electrical signal impulse generated by  $0.05V$  and  $0.15V$  input voltage peaks, respectively.

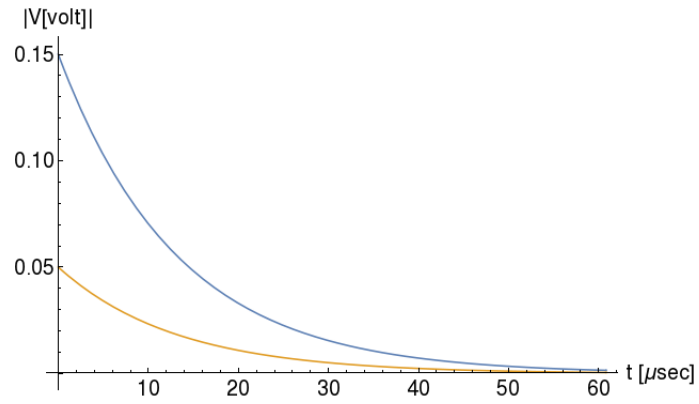


(a) Soliton propagation velocity in intracellular conditions.

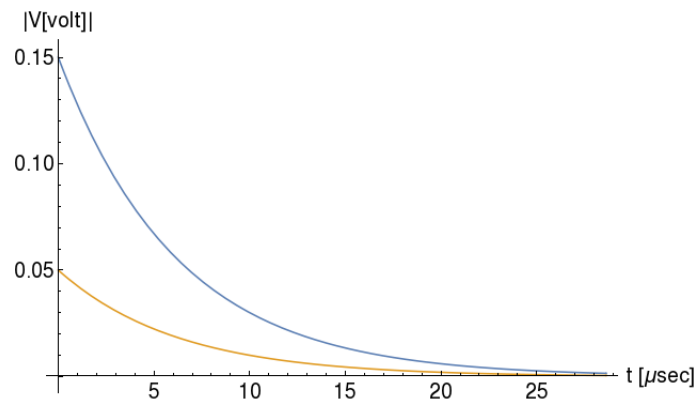


(b) Soliton propagation velocity in in-vitro conditions.

Figure 7: Orange and blue colors represent the propagation velocity of the electrical signal impulse generated by  $0.05V$  and  $0.15V$  input voltage peaks, respectively.



(a) Soliton peak attenuation in intracellular conditions.



(b) Soliton peak attenuation in in-vitro conditions.

Figure 8: Orange and blue colors represent the electrical signal impulse amplitude generated by  $0.05\text{V}$  and  $0.15\text{V}$  input voltage peaks, respectively.

voltage (soliton). The electrical impulse propagates upright and down for in-vitro and intracellular conditions, respectively.

Our results also show a significant influence of the voltage input on the electrical impulse shape, attenuation and kern propagation velocity. The filament is able to sustain the soliton propagation at almost constant kern velocity for the in-vitro condition, but it displays a remarkable deceleration for the intracellular condition, with a slower soliton peak attenuation which is more pronounced at higher voltage input. Solitons are narrower and travel faster at higher voltage input in the intracellular condition. Whereas the voltage input does not seem to play an important role on the soliton kern velocity in the in-vitro condition. On the other hand, the electrical impulse shape is wider at lower voltage input and the soliton range of the order of one micron in both electrolyte conditions. Although, the vanishing time is of around 2 times longer in the intracellular condition.

Overall, our results predict that the propagation of electrical signal impulses in the form of solitons are possible for a range of electrolyte solutions and voltage stimulus typically present in intracellular and in-vitro conditions. Our predictions are an improvement on less recent theories and in good agreement with experimentally obtained data for single filaments. One of the most important outcomes of this approach lies in the ability to determine the impact of molecular structure conformation (mutations) and physicochemical solution changes (protonations/deprotonations alterations) often present in pathological conditions in cytoskeleton filaments. This multi-scale theory may also be applicable to other highly charged rod-like polyelectrolytes with relevance in biomedicine and biophysics.<sup>3</sup> Currently we are working along this direction with the ultimate goal of providing a molecular understanding for how and why age and inheritance conditions induce dysfunction and malformation in cytoskeleton filaments associated with a variety of diseases.<sup>1</sup>

Our predictions are an improvement on less recent theories and in good agreement with experimentally obtained data for single filaments.

## Acknowledgments

This work was supported by NIH Grant 1SC2GM112578-01.

## 6. Appendix A

### 6.1. Numerical and Analytic Solution Comparison

We solve equation 35 numerically by using periodic boundary conditions  $W(\xi, \tau) = W(-\xi, \tau)$  and a voltage input signal:

$$W(\xi, 0) = -2\Omega_0^2 \text{sech}^2[\xi] \quad (48)$$

The artificially periodic boundary conditions were imposed to facilitate the resolution of the partial differential equation 35. However, for lengths of the microfilament big enough it does not affect the solution of the system.<sup>53</sup> The equation 35 was solved using the commercial software Mathematica 11.0.<sup>40</sup> We applied the numerical method of lines algorithm which is a efficient approach to numerically solve partial differential equations provided it is an initial value problem. This method discretizes all but one dimension, then integrates the semi-discrete problem as a system of Ordinary Differential Equations (ODEs) or Differential-Algebraic Equations (DAEs). Additionally, we configured some parameters to obtain the solution. We set the WorkingPrecision (e.g.

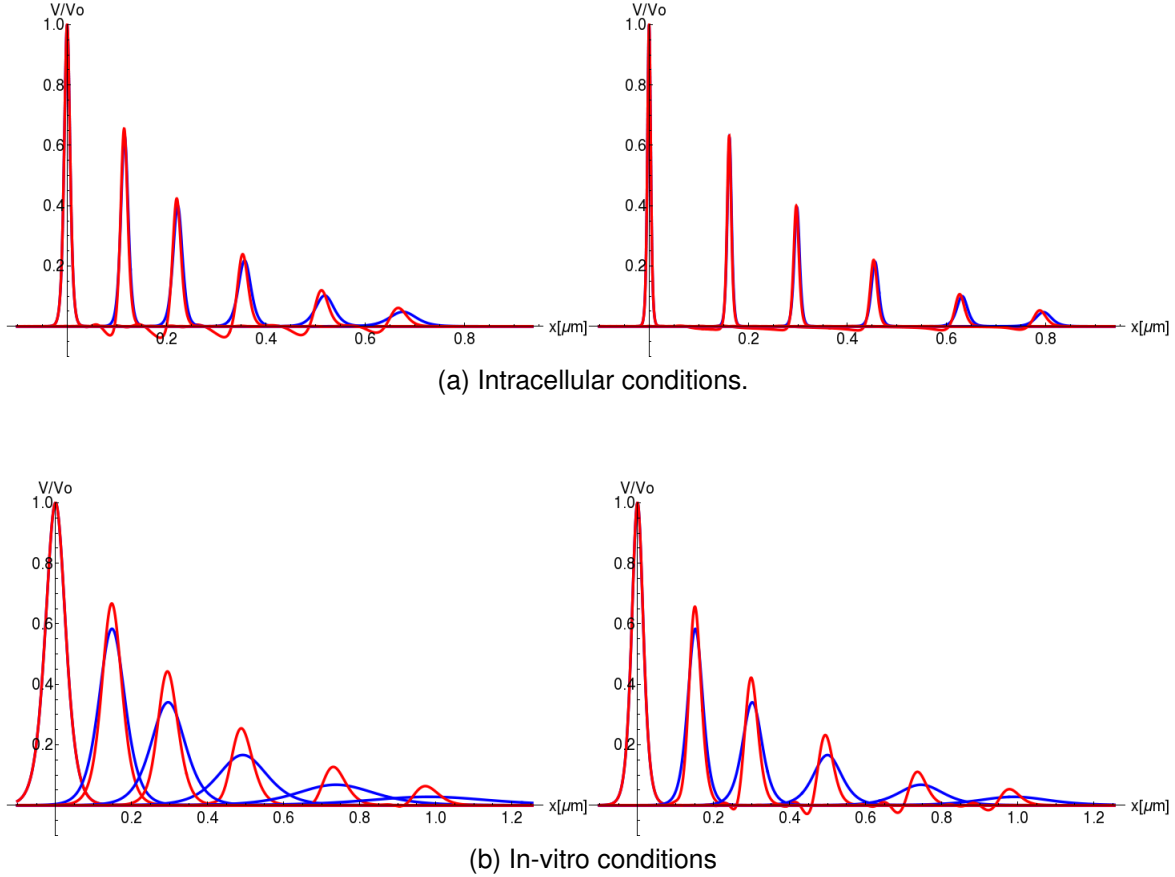


Figure 9: Comparison between numerical (red color) and analytic (blue color) solutions. The figures to the left and right sides correspond to the electrical signal impulse amplitude generated by  $0.05V$  and  $0.15V$  input voltage peaks, respectively. The electrical impulse peaks correspond to the snapshots mentioned in Fig. 6

how many digits of precision should be maintained in internal computations) to the MachinePrecision value (double-precision floating-point numbers:  $\approx 16$  decimal digits) . The AccuracyGoal and the PrecisionGoal (e.g. how many effective digits of accuracy and precision, respectively) were set to a value equal to half the setting for WorkingPrecision. The InterpolationOrder of the solution (e.g. continuity degree of the final output) was set to 6 for the  $\xi$  variable and 3 for the  $\tau$  variable. The MaxStepFraction (e.g. maximum fraction of the total range to cover in a single step) was equal to  $1/10$ , the MaxStepSize (e.g. maximum size of each step) was defined as the inverse of MaxStepFraction ( $10$ ) and the MaxSteps (e.g. maximum number of steps to take in generating a result) was set to  $10000$ . In the case of the NormFunction parameter, we used an infinity-norm.<sup>40</sup> It is worth mentioning that the inductance value considered in this work does not affect the numerical solution obtained for the soliton.

Fig. 9 shows the soliton profile comparison between the numerical and the approximate analytic solution (37) for both intracellular and in-vitro conditions, obtaining a good visual matching over the whole domain. In general, there was a short and intermediate time evolution where the adiabatic approximation is valid. Certainly, at longer times the perturbation increases the impact on the soliton shape and tails. Overall, the peak position and width, as well as the kern velocity between the numerical and analytic solutions in intracellular conditions, are in very good agree-



ment. Whereas, the analytic solution predicts a wider and more attenuated soliton for in-vitro conditions. Higher order approximations and multisoliton solutions will be considered in a future work.

## References

### References

- [1] C. dos Remedios and D. Chhabra. *Actin-Binding Proteins and Disease*. Protein Reviews. Springer New York, 2008.
- [2] N.J. Woolf and A. Priel. *Nanoneuroscience: Structural and Functional Roles of the Neuronal Cytoskeleton in Health and Disease*. Biological and Medical Physics, Biomedical Engineering. Springer Berlin Heidelberg, 2009.
- [3] Paul A. Janmey, David R. Slochower, Yu-Hsiu Wang, Qi Wen, and Andrejs Cebers. Polyelectrolyte properties of filamentous biopolymers and their consequences in biological fluids. *Soft Matter*, 10:1439–1449, 2014.
- [4] H.F. Cantiello, C. Patenaude, and K. Zaner. Osmotically induced electrical signals from actin filaments. *Biophysical Journal*, 59(6):1284 – 1289, 1991.
- [5] E.C. Lin and H.F. Cantiello. A novel method to study the electrodynamic behavior of actin filaments. evidence for cable-like properties of actin. *Biophysical Journal*, 65(4):1371 – 1378, 1993.
- [6] JE Goldman. Immunocytochemical studies of actin localization in the central nervous system. *Journal of Neuroscience*, 3(10):1952–1962, 1983.
- [7] Klaus Lange. Microvillar ion channels: Cytoskeletal modulation of ion fluxes. *Journal of Theoretical Biology*, 206(4):561 – 584, 2000.
- [8] Joachim Gartzke and Klaus Lange. Cellular target of weak magnetic fields: ionic conduction along actin filaments of microvilli. *American Journal of Physiology - Cell Physiology*, 283(5):C1333–C1346, 2002.
- [9] Mark Sundberg, Richard Bunk, Nuria Albet-Torres, Anders Kvennefors, Fredrik Persson, Lars Montelius, Ian A Nicholls, Sara Ghatnekar-Nilsson, Pär Omling, Sven Tågerud, et al. Actin filament guidance on a chip: toward high-throughput assays and lab-on-a-chip applications. *Langmuir*, 22(17):7286–7295, 2006.
- [10] Mark E. Arsenault, Hui Zhao, Prashant K. Purohit, Yale E. Goldman, and Haim H. Bau. Confinement and manipulation of actin filaments by electric fields. *Biophysical Journal*, 93(8):L42 – L44, 2007.
- [11] Rémi Galland, Patrick Leduc, Christophe Guérin, David Peyrade, Laurent Blanchoin, and Manuel Théry. Fabrication of three-dimensional electrical connections by means of directed actin self-organization. *Nature Materials*, 12(5):416–21, May 2013. A Press release CEA, CNRS, UJF, INRA has been published for this publication (February 11th, 2013): <http://www2.cnrs.fr/presse/communique/2987.htm>.

- [12] Fernando Patolsky, Yossi Weizmann, and Itamar Willner. Actin-based metallic nanowires as bio-nanotransporters. *Nature Materials*, 3(10):692–5, 10 2004. Copyright - Copyright Nature Publishing Group Oct 2004; Last updated - 2014-04-30.
- [13] Till Korten, Alf Månsson, and Stefan Diez. Towards the application of cytoskeletal motor proteins in molecular detection and diagnostic devices. *Current Opinion in Biotechnology*, 21(4):477 – 488, 2010.
- [14] Fumio Oosawa. Counterion fluctuation and dielectric dispersion in linear polyelectrolytes. *Biopolymers*, 9(6):677–688, 1970.
- [15] Gerald S. Manning. The molecular theory of polyelectrolyte solutions with applications to the electrostatic properties of polynucleotides. *Quarterly Reviews of Biophysics*, 11(2):179–246, 1978.
- [16] G. S. Manning. Limiting Laws and Counterion Condensation in Polyelectrolyte Solutions I. Colligative Properties. *J. Chem. Phys.*, 51:924–933, August 1969.
- [17] Bruno H. Zimm. *Use of the Poisson-Boltzmann Equation To Predict Ion Condensation Around Polyelectrolytes*, chapter 17, pages 212–215. 1986.
- [18] Joseph A Kolosick, Don L Landt, HCS Hsuan, and Karle E Lonngren. Properties of solitary waves as observed on a nonlinear dispersive transmission line. *Proceedings of the IEEE*, 62(5):578–581, 1974.
- [19] A. Noguchi. Solitons in a nonlinear transmission line. *Electronics Communications of Japan*, 57:9 – 13, Feb 1974.
- [20] Karl E. Lonngren. Observations of solitons on nonlinear dispersive transmission lines. In Karl Lonngren and Alwyn Scott, editors, *Solutions in Action*, pages 127 – 152. Academic Press, 1978.
- [21] S. Novikov, S.V. Manakov, L.P. Pitaevskii, and V.E. Zakharov. *Theory of Solitons: The Inverse Scattering Method*. Plenum, New York, 1984.
- [22] Marc Le Bret and Bruno H. Zimm. Distribution of counterions around a cylindrical polyelectrolyte and manning's condensation theory. *Biopolymers*, 23(2):287–312, 1984.
- [23] John Newman. *Electrochemical Systems*, chapter 1. Englewood Cliffs, N.J. Prentice-Hall, 1973.
- [24] J.A. Tuszyński, S. Portet, J.M. Dixon, C. Luxford, and H.F. Cantiello. Ionic wave propagation along actin filaments. *Biophysical Journal*, 86(4):1890 – 1903, 2004.
- [25] M. V. Satarić, D. I. Ilić, N. Ralević, and Jack Adam Tuszynski. A nonlinear model of ionic wave propagation along microtubules. *European Biophysics Journal*, 38(5):637–647, Jun 2009.
- [26] D. L. Sekulić, B. M. Satarić, J. A. Tuszyński, and M. V. Satarić. Nonlinear ionic pulses along microtubules. *The European Physical Journal E*, 34(5):49, 2011.

- [27] D. L. "Sekulić and B. M. Satarić. An improved nanoscale transmission line model of micro-tubule: The effect of nonlinearity on the propagation of electrical signals. *Facta Universitatis, Series: Electronics and Energetics*, 28(1):133–142, 2015.
- [28] Alexei A. Kornyshev. Double-layer in ionic liquids: Paradigm change? *The Journal of Physical Chemistry B*, 111(20):5545 – 5557, 2007.
- [29] De en Jiang, Dong Meng, and Jianzhong Wu. Density functional theory for differential capacitance of planar electric double layers in ionic liquids. *Chemical Physics Letters*, 504(4):153 – 158, 2011.
- [30] Stanislaw Lamperski, Monika Pluciennik, and Christopher W. Outhwaite. The planar electric double layer capacitance for the solvent primitive model electrolyte. *Phys. Chem. Chem. Phys.*, 17:928–932, 2015.
- [31] Vadim Warshavsky and Marcelo Marucho. Polar-solvation classical density-functional theory for electrolyte aqueous solutions near a wall. *Physical Review E - Statistical, Nonlinear, and Soft Matter Physics*, 93(4), 4 2016.
- [32] Yao Cong, Maya Topf, Andrej Sali, Paul Matsudaira, Matthew Dougherty, Wah Chiu, and Michael F. Schmid. Crystallographic conformers of actin in a biologically active bundle of filaments. *Journal of Molecular Biology*, 375(2):331 – 336, 2008.
- [33] John Newman. *Electrochemical Systems*, chapter 9. Englewood Cliffs, N.J. Prentice-Hall, 1973.
- [34] Zaven Ovanesyan, Bharat Medasani, Marcia O Fenley, Guillermo Iván Guerrero-García, Mónica Olvera de la Cruz, and Marcelo Marucho. Excluded volume and ion-ion correlation effects on the ionic atmosphere around b-dna: Theory, simulations, and experiments. *The Journal of chemical physics*, 141(22):225103, 2014.
- [35] Bharat Medasani, Zaven Ovanesyan, Dennis G Thomas, Maria L Sushko, and Marcelo Marucho. Ionic asymmetry and solvent excluded volume effects on spherical electric double layers: A density functional approach. *The Journal of chemical physics*, 140(20):204510, 2014.
- [36] Christian Hunley and Marcelo Marucho. Electrical double layer properties of spherical oxide nanoparticles. *Phys. Chem. Chem. Phys.*, 19:5396–5404, 2017.
- [37] Zaven Ovanesyan, Amal Aljzmi, Manal Almusaynid, Asrar Khan, Esteban Valderrama, Kelly L. Nash, and Marcelo Marucho. Ion-ion correlation, solvent excluded volume and ph effects on physicochemical properties of spherical oxide nanoparticles. *Journal of Colloid and Interface Science*, 462(Supplement C):325 – 333, 2016.
- [38] Todd J. Dolinsky, Jens E. Nielsen, J. Andrew McCammon, and Nathan A. Baker. Pdb2pqr: an automated pipeline for the setup of poisson-boltzmann electrostatics calculations. *Nucleic Acids Research*, 32(suppl 2):W665 – W667, 2004.

- [39] Neil R. Voss and Mark Gerstein. 3v: cavity, channel and cleft volume calculator and extractor. *Nucleic Acids Research*, 38(suppl 2):W555–W562, 2010.
- [40] Wolfram Research, Inc. *Mathematica Version 11.0*, 2016.
- [41] Yizhak Marcus. Ionic radii in aqueous solutions. *Chemical Reviews*, 88(8):1475–1498, 1988.
- [42] David C. Grahame. The electrical double layer and the theory of electrocapillarity. *Chemical Reviews*, 41(3):441–501, 1947. PMID: 18895519.
- [43] D. L. Sekulić and M. B. Zivanov. Computational study on soliton-like pulses in the nonlinear rlc transmission lines. In *2012 Proceedings of the 35th International Convention MIPRO*, pages 228–232, May 2012.
- [44] M. Ablowitz and H. Segur. *Solitons and the Inverse Scattering Transform*. Society for Industrial and Applied Mathematics, 1981.
- [45] V.I. Karpman and E.M. Maslov. A perturbation theory for the korteweg-de vries equation. *Physics Letters A*, 60(4):307 – 308, 1977.
- [46] A. J. Mohamad Jawada. Soliton solutions of a few nonlinear wave equations in engineering sciences. 2014.
- [47] V. I. Karpman and E. M. Maslov. Perturbation theory for solitons. *Zh. Eksp. Teor. Fiz.*, 73:537–, August 1977.
- [48] M. A. Allen and G. Rowlands. A solitary-wave solution to a perturbed kdv equation. *Journal of Plasma Physics*, 64(4):475–480, 2000.
- [49] V I Karpman. Soliton evolution in the presence of perturbation. *Physica Scripta*, 20(3-4):462, 1979.
- [50] E. M. Maslov. Perturbation theory for solitons in the second approximation. *Theoretical and Mathematical Physics*, 42:237–245, 1980.
- [51] H. Lodish, A. Berk, SL. Zipursky, H. Lodish, P. Matsudaira, D. Baltimore, and J. Darnell. *Molecular Cell Biology. 4th edition*, chapter Section 15.4, Intracellular Ion Environment and Membrane Electric Potential. New York: W. H. Freeman, 2000.
- [52] E. Afshari and A. Hajimiri. Nonlinear transmission lines for pulse shaping in silicon. *IEEE Journal of Solid-State Circuits*, 40(3):744–752, March 2005.
- [53] Jan Ole Skogestad and Henrik Kalisch. A boundary value problem for the kdv equation: Comparison of finite-difference and chebyshev methods. *Mathematics and Computers in Simulation*, 80(1):151 – 163, 2009. Nonlinear Waves: Computation and Theory {VII}.